Growth and isolation of large area boron-doped nanocrystalline diamond sheets: A route towards diamond-graphene heterojunction

R. Bogdanowicz[1], M. Ficek[1], M. Sobaszek[1], A. Nosek[2], Ł. Gołuński[1], J. Karczewski[3], A. Jaramillo-Botero[4], W.A. Goddard III[4], M. Bockrath[2] and T. Ossowski[5]*

Prof. R. Bogdanowicz* Corresponding-Author,
Department of Metrology and Optoelectronics, Faculty of Electronics, Telecommunications and Informatics, Gdansk University of Technology, 11/12 G. Narutowicza St., 80-233 Gdansk, Poland
E-mail:rbogdan@eti.pg.edu.pl

M. Ficek, Dr. M. Sobaszek, Ł. Gołuński,
Department of Metrology and Optoelectronics, Faculty of Electronics, Telecommunications and Informatics, Gdansk University of Technology, 11/12 G. Narutowicza St., 80-233 Gdansk, Poland

A. Nosek, Prof. M. Bockrath
Department of Physics, University of California Riverside, 900 University Avenue, Riverside, California 92521, USA

Dr. J. Karczewski
Faculty of Applied Physics and Mathematics, Gdansk University of Technology, 11/12 G. Narutowicza St., 80-233 Gdansk, Poland

Dr. A. Jaramillo-Botero, Prof. W.A. Goddard III (ORCID:0000-0003-0097-5716)
Materials and Process Simulation Center, California Institute of Technology, Pasadena, California 91125, USA

Prof. T. Ossowski
Department of Analytical Chemistry, Faculty of Chemistry, University of Gdansk, 63 Wita Stwosza St., 80-952 Gdansk, Poland

Keywords: chemical vapor deposition; freestanding diamond nanosheets; graphene; heterojuction; carrier transfer

Many materials device applications would benefit from thin diamond coatings, but current growth techniques, such as chemical vapor deposition (CVD) or atomic layer deposition (ALD), require high substrate and gas-phase temperatures that would destroy the device being coated. We report here, the development of free-standing, thin boron-doped diamond nanosheets grown on tantalum foil substrates via microwave plasma assisted CVD. These diamond sheets (measuring up to 4 x 5 mm in planar area, and 300-600 nm in thickness) were removed from the substrate using mechanical exfoliation and then transferred to other substrates, including Si/SiO_2 and graphene. We characterized the electronic properties of the resulting diamond nanosheets and their dependence on the free-standing growth, the mechanical exfoliation and transfer processes, and ultimately on their composition. To validate this, we developed a prototype diamond nanosheet – graphene FET transistor (DNGfet) and studied its electronic transport properties, as a function of temperature. The resulting DNGfet device exhibited thermally activated transport (thermionic conductance) above 20 K. These findings demonstrate, for the first time, a low temperature diamond-based transistor.

1. Introduction

Carbon-based layered materials are of considerable interest as potential electronic materials for use in future electronic and optoelectronic devices, including transistors, photodetectors, and optical modulators.

In addition to the expected high performance electronic properties, the high transparency of thin CVD diamond films over the range of ultraviolet to far-infrared spectral regions, would enable novel technological applications to optical coatings,[1,2] optoelectronic switching devices,[3] or high-speed near-infrared photodetectors.[4]

However, these applications are limited by the nature of CVD growth of diamond. Here, we propose and validate the use of free-standing nanocrystalline diamond (NCD) foils and thin diamond nanosheets to overcome this problem. We show that our thin diamond material can be transferred to other substrates by standard scotch-tape techniques employed in 2D materials and multi-layered electronic devices. Furthermore, our free-standing undoped non-conductive diamond films can be applied as a dielectric barrier while their boron-doped counterparts serve as a semiconducting p-type layer or as a biosensing surface. This enables application of diamond to graphene transistors that could circumvent problems associated with Joule heating and subsequent velocity saturation in graphene when linked to SiO_2 substrates. Moreover, the our films retain the high phonon energy of 65 meV in diamond , which could also improve the R.F. performance of graphene transistors.[5]

A few attempts to fabricate a diamond foil have been reported in the literature. Seshan *et al.*[6] demonstrated a versatile transfer technique based on an all-dry visco-elastic stamping to pick up NCD films grown by CVD that were later thinned by wet and plasma etching (as thin as 55 nm; typically 50×50 μm in size). Next, Behroudj *et al.* fabricated the diamond foils on a Si_3N_4 membranes or Si wafers etched back in KOH to release it from the substrate. They reported that the final selecting of the diamond films out of the KOH etchant was challenging mainly because the films fractured.[7]

Lodes *et al.*[8] and Fecher *et al.*[9] reported use of a Nd:YAG laser to strip-off films of hot-filament CVD grown diamond. However, the thickness of those nano- and micro-crystalline diamond (NCD) foils had to be at least 30 μm, in order to enable stripping with a laser. Moreover, Lodes *et al.* studied mechanical properties of NCD foils (e.g. fracture strength, Young's moduli) by means of Weibull analysis. They demonstrated that thick NCD foils can be manufactured with high reliability, and that the foils offer fracture strength far greater than

that of conventional technical ceramics.[8,10,11] Furthermore, Sobolewski *et al.*[12] examined the surface energy of free-standing NCD foils and the effect of surface treatment by various liquids. The pre-treatment with ethanol was found to provide an ideal cleaning procedure. The thermoelectric transport properties of boron-doped nanocrystalline diamond foils were studied by Engenhorst *et al.*[13] They reported satisfactory values of power factors, i.e. $>10^{-4} Wm^{-1} K^{-2}$ at 900°C despite the low mobility of charge carriers (ca. 1 $cm^2 V^{-1} s^{-1}$). However, the NCD foils suffer from carrier scattering associated with their high thickness of several tens of microns, which limits the tunneling of charges.

Thus, to date, there is no report of fabricating large-area thin diamond nanosheets with nanoscale thickness. In the present paper, we describe for the first time, the procedure for fabricating thin diamond foils/nanosheets that could be used in electronic heterostructural systems. We also demonstrate the assembly of a novel diamond-on-graphene heterojunction, displaying thermally-activated transport. Moreover, we present a detailed study of both growing and transferring diamond nanosheets, and report on their unique carrier transport properties from Hall effect measurements, along with their molecular structure and surface morphology.

2. Discussion and results

2.1. Mechanism of diamond nanosheet delamination at tantalum substrate simulated by molecular dynamics

We used molecular dynamics (MD) simulations to determine the specific phenomenon of the diamond nanosheet delamination. Several mechanisms are responsible for the adhesion of thin film to the substrates. The combination of different theories (e.g. mechanical, chemisorption, diffusion adhesion) must to be discussed to explain the observed lack of adhesion at the interface between the CVD diamond and tantalum foils.

The mechanical adhesion is based on the roughness and porosity of the substrate surface, thus polished tantalum foils were utilized to minimize this factor. Next, chemisorption is limited by the higher energy of the Ta-C covalent bond compared to C-C bonds in the CVD diamond film (see **Figure 1C**). The growth of Ta-C layer needs 6.203 eV (to add another C layer at tantalum – 7.048 eV), while C-C diamond surface requires only 7.79 eV (to add another C add layer in diamond – 7.803 eV) at a temperature of 1000 K, which is similar to the conditions of CVD growth. Our estimated energetics are comparable with those reported by Winter *et al.* [14] for C-C or Ta-C derived by Yan *et al.*.[15] Moreover, the metallic Ta-Ta bond is "softer" than the covalent Ta-C in tantalum carbide or the C-C bonds in diamond. Ta-C dissociation would normally happen at much higher temperatures since the melting point of tantalum carbide is around 3880^{o}C.

Our studies of van der Walls (vdW) interactions revealed minor adhesive forces in the system as illustrated in **Figure 1B**. The repulsive forces were predicted for Ta – CVD diamond interface, which can be related to the diverged Hamaker constants resulting from different dielectric response functions of those materials.[16]

Figure 1

Besides the aforementioned theoretical studies, the main phenomena underlying CVD diamond delamination are thermally induced interfacial stress and lattice mismatch. Firstly, the lattice mismatch between tantalum (a = 3.30 Å) and diamond (a = 3.57 Å) is rather large (approx. 7%), which leads to initial stresses that prohibit proper adhesion of diamond. Secondly, the difference in the thermal expansion coefficients of diamond (1 x 10^{-6} K^{-1}) and tantalum (6.5 x 10^{-6} K^{-1}) at 27 °C seems to have minor impact. During the diamond growth process at 700°C,

the thermal expansion coefficient increases to 8 x 10^{-6} K^{-1} for tantalum,[17] while for diamond, it shifts only to 4 x 10^{-6} [K^{-1}].[18] This difference allows the diamond nanosheet to shrink slightly less than the tantalum substrate, making it a minor diamond delamination factor.

The atomistic simulations predicted deformations of Ta (110) – Diamond (111) interface, as presented in **Figure 1A**. The top side image shows the initial phase of system (0 ps). Next, the slab was heated to 1000 K (50 ps) revealing the dissociation of existing Ta-C bonds and slight deformation of both lattices. During the additional 50 ps (see the back side image in **Figure 1A**) the slab was cooled down to 300 K. The deformation and defects of diamond lattice are evident, which can be attributed to the lower dissociation energy of C-C bond compared to Ta-Ta bond.[19]

In general, several high adhesion spots still existed, limiting the area of nanosheet delamination. We attribute the adherence spots mainly to the non-diamond phases growing at the interface during the nucleation process. They are characterized by high porosity and roughness that contribute significantly to minimization of the interfacial stress. Nevertheless, this stage of our procedure needs further experimental investigation to find optimum parameters for CVD growth (e.g. by using dynamic variations of the methane admixture).

2.2. Diamond nanosheets: surface properties and film composition

We characterized the surface morphology and profile of the diamond sheets by high-resolution SEM and AFM imaging techniques. First, the diamond nanosheet was transferred to a non-conductive Si/SiO_2 substrate (**Figure 2A**). The analyzed diamond nanosheets were approximately 4 x 5 mm in size and *ca.* 600 nm thick (see **Figure 2B**).

Figures 2C and **2D** show the AFM surface profile of the diamond sheets. The edges of transferred samples are smooth and sharp. Based on AFM measurements, the estimated surface roughness was 96 nm. The top side (the plasma facing surface) of diamond sheet is shown in

Figure 2E, while its back side (the substrate facing surface), in **Figure 2F**. The difference between the top and back sides of diamond sheet is clearly visible. It can be explained by the fact that the back side contains more non-diamond carbon phases present in the early stage of growth. Furthermore, the lattice mismatch between the tantalum substrate and diamond and the difference in thermal expansion coefficients resulting in low adhesion, may play a role.

Figure 2

Grains with a radius < 100 nm are marked in red color (**Figure 2E and 2F** - right) on the both sides of diamond nanosheets. Hence, the calculated mean grain radius for the top and back sides of nanosheet are ca. 50 and 70 nm, respectively. The average area of the grains also differs between top and back side. For the back side 94% of the grains have anarea below 0.06 μm^2 while it is only 75% for the top side. On the other hand, for top side grains 25% have areas above 0.06 μm^2 with some grains area up to 0.14 μm^2, whereas the back side has nograins with areas above 0.1 μm^2. The crystallites present on the top surface are clearly visible, but those on the backside of the nanosheet seem to be flat and smooth (**Figure 3A.1 and 3B.1**). Such differences in texture between the top and backsides of diamond films has previously been described in the literature.[20] We attribute this to the high nucleation density at the initial stage. Next, the top surface leads mainly to (111) facets, while on the nucleation side the tantalum substrate promotes (100) facets in the initial stage of growth, so that (100) facets dominate. However, during growth the crystals change to (111) facets due to increased free space and higher temperature associated with the growth kinetics.[21] Some black spots visible in microimages in **Figure 2F** and **Figure 3B** are attributed to agglomerated diamond seeds

originating from seeding slurry or the growth of interface defects during the initial phase of CVD process.

Figure 3

The measured wettability of the back side of diamond sheet was xx°, which is 21° higher than that of the top side. However, the impact of different surface morphology of the two sides of diamond sheet is negligible.[22] The biggest impact on wettability is attributable to the hydrogenated top surface due to hydrogen plasma deposition, thus hydrogen termination is responsible for surface hydrophobicity.[23]

We find Raman spectroscopy to be a useful tool for these CVD diamond studies, offering fingerprint-like spectra showing a narrow diamond line at 1332 cm^{-1} at room temperature. The Raman spectra of diamond nanosheets are summarized in **Figure 4**. The nanosheet samples were isolated from the tantalum substrates and then transferred to thick silicon oxide wafers to undergo Raman investigation (see **Figure 4A**). The microscopic images exhibited the smooth diamond surface with partial textural imprints on the backside of the sheet, which were mirroring the morphology of tantalum surface.

Figure 4

Surprisingly, the spectra did *not* reveal a typical Fano effect, moreover the band at 480 cm^{-1} attributed to boron-doping the was not observed in our studies (range not shown in the graph to avoid strong Si line). Both sides of the diamond sheet displayed characteristic nanocrystalline features, although the film had been grown using typical conditions for microcrystalline highly

boron-doped diamond.[24] This effect may result from the specific structure and texture of the substrate and the type of seeding prior to CVD.

Comparison of Raman spectra recorded for the both sides of diamond sheet (see **Figure 4B**) revealed the high coherence of the molecular structure. The recorded spectra showed four major Raman peaks and bands at 1150, 1331, 1460-1560 and 2800-3000 cm^{-1}. The spectra were deconvoluted to give deeper insight into these peaks, as shown in **Figures 4C** and **4D**. The experimental Raman curves were fitted by using Lorentzian-Gaussian distributions estimated by means of Origin Pro 9.0 software.

The experimental and fitted spectra showed the presence of a dominant first-order diamond Raman line at 1331 cm^{-1} with a full-width half-maximum of 2.1 cm^{-1}, which is related to the vibrations of two interpenetrating cubic sublattices.[25] It is noteworthy that the diamond peak was slightly shifted towards lower values by around 2 cm^{-1}. This phenomenon was reported as dependent on temperature and applied stress.[26] Moreover, the diamond peak was broader and thus interfered with the 1334 cm^{-2} line assigned to the sp^2 amorphous carbon, a so-called "D" band.

The presence of nanocrystalline diamond was proved by the contribution of the ~1164 cm^{-1} band, which is mostly attributable to the transpolyacetylene at grain boundaries.[27] Such a band position was reported by Rudiger *et al.*[28] for nanocrystalline diamond excited with a green laser. In our study, another band with a maximum at 1454 cm^{-1} was also related to the same carbon phase because both the aforementioned bands are typically recorded in nanocrystalline CVD diamond films.

The diamond nanosheet also included sp^2 amorphous carbon, which contributed to the "G" peak at 1525 cm^{-1}. The signal was associated with the single-crystal graphite forms and carbon-carbon stretching modes.

The integrated areas under the first-order diamond line and G band were used to estimate the sp^3/sp^2 ratios for the top and bottom sides of nanosheet (see inset values in **Figures 4CD**). We note that the sp^3/sp^2 ratio for the top side of nanosheet was two times smaller than that for the bottom side. The pronounced G band identified in the top surface indicates the increased sp^2 carbon contribution at the grain boundaries. As previously reported,[29] this finding can be attributed to higher graphitization at the intragrain regions. The above conclusion is in agreement with the SEM analysis, which revealed the small intragrain clusters, along with lower values of resistivity for the top side of the diamond nanosheet (see **Table 1**). The black spots observed in the SEM images (**Figure 3B**) were not assigned to any specific fingerprint in the Raman spectrum.

The broad multi-band positioned in the 2800 3000 cm^{-1} region was attributed to the C-H Raman stretching band (**see Figure 4B**), which suggests that the (100) facets were dominantly terminated with C–H monohydride species.[25]

2.3. Electronic characterization of isolated diamond nanosheets

The four-point probe technique was used to measure the resistivity of the both sides of diamond nanosheet transferred to the thick oxide wafer substrates. The resistivity of the back side of the sample reached 71 Ω cm, while the top surface showed a value of 0.32 Ω cm. The effect of higher resistivity in the back side of diamond sheet can be explained by boron suppression by oxygen and the contribution of the undoped seeds to the charge diffusion in the initial stage of CVD growth, as reported by Tsigkourakos *et al.*.[30] The typical BDD electrodes display resistivity that is similar to that of the top side of diamond nanosheet. This, in turn, suggests a similarity in the boron doping or charge transfer mechanism of diamond sheets.[24]

Table 1

Furthermore, Hall effect measurements in the van der Pauw geometry were performed to compare the mobility and carrier density of the top and bottom sides of the obtained diamond sheet. The carrier density of the top surface exhibited typical semiconducting properties at ca. 3.1 x 10^{17} /cm^3 and 62 cm^2/Vs, as listed in Table 1. In contrast, the back side of the diamond nanosheet delivered a much smaller carrier density of 1.67 x 10^{14}/cm^3. The observed discrepancy most likely results from the boron suppression effect in the initial stage of CVD growth.

Moreover, the back side of the nanosheet displayed higher-quality diamond with smaller crystals and no defective intergrain regions in comparison to top side. The defective boron-rich areas are responsible for the most effective pathways for charge transport and a decrease in resistivity.[29,31,32] Lu *et al.* reported that boron mainly accumulates along the grain boundaries of polycrystalline diamond.[33] Also, boron tends to occupy the (111) facets,[34,35] while the back sides of our nanosheets were characterized by the presence of texture rich in the (100)-like facets (see **Figure 4B**). We consider that the smaller crystals of back side of the nanosheet , it is responsible for the high charge mobility (532 cm^2/Vs), which is one order of magnitude higher than that of nanocrystalline top surface (rich in impurity centers causing perturbations in carrier transfer).[36]

Figure 5

2.4. Diamond-graphene heterojunction investigation

In order to investigate the contact between diamond and graphene, we fabricated a diamond-on-graphene heterostructural device. To this end, CVD grown graphene was transferred onto a Si/SiO_2 chip. The diamond nanosheet was placed on the chip to be in contact with both the

CVD graphene and SiO_2 chip surface. A previous report found that graphene preserves its sp^2 bond structure on top of insulating diamond[37], rather than forming covalent bonds between graphene and diamond. Strong van der Waals forces are the predominant mechanism through which our diamond-on-graphene junction is formed. **Figure 5A** shows the optical image of the fabricated device, in particular graphene, diamond, and attached contacts. A schematic diagram of the circuit is presented in **Figure 5B**.

The Ohmic contacts enabled us to apply a voltage across the diamond-on-graphene interface as well as across the top surface of the diamond nanosheet. The resistance values recorded on the top surface between contact 1 and contact 2 (see **Figure 5A**) followed a linear distribution, while the measured values of *R*, after subtracting the wiring of the electronic setup, were 90 and 1300 **Ω** at room temperature and T = 4.2 K, respectively.

The low bias resistance of the diamond-on-graphene heterojunction varied from 22.05 k**Ω** at room temperature to *ca.* 4 M**Ω** at 4.2 K. The strong temperature dependence and relatively high value of the resistance indicates that the series resistance of the graphene sheet and diamond can be neglected, that is, the dominant resistance in the circuit was the heterojunction.

The resulting transport characteristics of the heterojunction under high vacuum (see **Figure 5C**) showed current-voltage (*I-V*) variations in relation to temperature *T*. These characteristics were nonlinear, and under low-bias conditions, the linear response conductance *G* decreased with decreasing *T*. **Figure 5D** plots the measured conductance *G vs. 1/T*, where G was extracted from each trace and expressed as a natural logarithm. The inverse conductance data followed an approximately linear distribution for high *T* values, and reached a constant level for low *T* values. This is characteristic of the thermally activated transport over a barrier, as shown in the schematic diagram in the upper inset in **Figure 5C**, with the transport dominated by quantum tunneling at temperatures below T = 20K. The slope analysis of the activation plot from the

diamond-on-graphene heterostructure yielded an energy barrier E_A = 17.28 meV from the fitted slope $-E_A / k_B$ = -200.54K. Additional measurements of just graphene and just the diamond surface are included in the inverse conductance data. Over the whole temperature range the diamond surface resistivity is three orders of magnitude smaller than the diamond-on-graphene heterojunction. Graphene exhibits a typical constant semi-metallic behavior in the Arrhenius plot with no thermally activated conductance while the diamond surface shows an energy barrier of E_A = 12.46 meV with a slope of $-E_A / k_B$ = -144.55K. The constant activation energies above 50K are consistent with a nearest-neighbor hopping conduction mechanism of the form $\sigma(T) = \sigma_0 \, exp(-E_A/k_BT)$ through an impurity band induced by the boron doping.

We observe a non-constant activation energy below 50K[38], indicating a crossover towards variable rang-hopping .

Our results lead to a novel sp^3-on-sp^2 carbon technological approach that provides an attractive alternative to the graphene-on-diamond devices. [37] We consider that this provides a significant impact for graphene applications in high power, high-frequency transistors, and biosensing FETs.

3. Conclusion

We have fabricated a novel diamond material in the form of ultra-thin nanosheets by using a microwave plasma-assisted CVD process. We were able to isolate free-standing nanosheets due to the unique lack of adhesion during the diamond growth on the polished tantalum foil. Our atomistic simulations of thermal deformations of Ta (110) – Diamond (111) interface reveal the mechanism behind the observed phenomenon. We established that the main factor responsible for CVD diamond delamination is thermally induced interfacial stress and lattice mismatch. The lattice mismatch between the two materials and differing thermal expansion

coefficients enabled mechanical isolation and transfer of large-area diamond nanosheets to various secondary substrates, including temperature-sensitive substrates.

We find that the sp^3/sp^2 ratio of the top side of the obtained nanosheet is smaller than that of the bottom side. We attribute this to the elevated boron concentration during doping, which we later confirmed by the SEM analysis, revealing small intragrain clusters, as well as a lower resistivity in the top side of the nanosheet. Non-uniform boron concentration along the depth profile resulted from the boron suppression by residual oxygen and the contribution of the undoped seeds to the charge diffusion in the initial stage of CVD growth.

In summary, we investigated the electrical and thermal properties of prototypical diamond-on-graphene FET transistor fabricated by using nanosheets. We found thermally activated transport over a barrier, with the transport dominated by quantum tunneling at low T. These findings demonstrate, for the first time, a low temperature diamond-based transistor.

Experimental Section

CVD growth of diamond films: The boron-doped diamond nanosheets were synthesized in an MWPACVD system (SEKI Technotron AX5400S) on mirror-polished tantalum foils (Sigma-Aldrich Chemie, 0.025 mm thick, 99.9+% metal basis). Substrates were seeded by means of spin-coating at 3000 rpm for 2 min.[39] A diamond slurry (consisting of nanodiamond particles of 4-7 nm in size) was prepared in the laboratory in dimethyl sulfoxide (DMSO) with 1% of polyvinyl alcohol (PVA) added. The temperature of the heated graphite stage was kept at 500°C during the deposition process. The CH_4:H_2 molar ratio of the mixture in this study was set at 1% of gas volume at 300 sccm total flow rate. The doping level of boron in the gas phase, expressed as the [B]/[C] ratio, was 10,000 ppm. Diborane (B_2H_6) was used as the dopant precursor. The optimized plasma microwave power of 1000 W was applied during the synthesis

of diamond sheets. The growth time was 120 min, which resulted in polycrystalline foil with a thickness of approximately 600 nm.

Figure 6

Isolation and transfer of diamond sheets: The boron-doped diamond sheets grown on tantalum showed low adhesion to the substrate, as illustrated in **Figure 6A**. In order to release large diamond sheets from the tantalum substrate, the as-grown sample was put into deionized water, but without submerging the diamond layer. Next, the diamond nanosheets were isolated mechanically from tantalum substrate (see **Figure 6B**).

The floating diamond sheets were transferred to a secondary substrate by positioning the substrate under the diamond sheet and pulling it out from the water. Due to intrinsic stress in the film, the free-standing diamond nanosheets tend to roll up during a dry release process. The use of polar solvent, such as water, provides additional tension that enhances the transfer of large diamond sheets and improves their adhesion to the surface of secondary substrate, e.g. thick thermal SiO_2 on Si wafer (Si/SiO_2, see **Figure 6C**).

Theoretical basis and DFT modeling protocols: We used atomistic model structure to validate the stress properties and delamination mechanism of diamond at the interface with tantalum. We prepared the model using the molecular builder in Virtual NanoLab, version 2015.2 (QuantumWise A/S). Then we optimized the model structures using Density Functional Theory (DFT) with a local density approximation (LDA) exchange-correlation.[40]. We allowed spin-polarization with a plane wave cutoff of 400 eV. Structures were optimized using conjugate gradient minimization, with convergence set to a maximum force of $1e^{-4}$ eV/Å or an energy difference of $1e^{-4}$ eV/Å.

The same level of DFT was used to estimate stress and interface bonding properties using the program Atomistix ToolKit version 2015.2, QuantumWise A/S (www.quantumwise.com). [41,42] For the Brillouin-zone integration, a Monkhorst-Pack scheme sampled with 1×1×50 k-points was utilized,[43] and a single-zeta (SZ) basis set was used with a mesh cutoff at 150 Ry. Molecular dynamics (MD) simulations were performed by means of LAMMPS (Large-scale Atomic/Molecular Massively Parallel Simulator) package.[44] The accuracy of molecular dynamics predictions for a particular structure is strongly dependent on the accuracy of the force fields for describing the interatomic forces. In this work, we used the ReaxFF potentials[45–47] to introduce the bonding interactions between the carbon and tantalum atoms. The relaxed and equilibrated Ta (110) - diamond (111) structure was heated to 1000 K for 50 ps and then cooled down to 300 K for over 50 ps by using a Nose–Hoover thermostat that maintains the pressure of 0 bar in all directions. Simulations are started at 0K to confirm initial structure is in agreement with crystallographic data, followed by a simulated annealing process (fast heating and slow cooling) to obtain a thermodynamically stable (and realistic) structure at room temperature.

Since the polycrystalline BDD electrodes fabricated by CVD methods are usually dominated by (111) planes,[48] we selected this surface for the DFT analysis of delamination mechanism (see **Figure 1A**). Commercial tantalum substrates would likely have a rough surface with different crystallographic planes. Nevertheless, we restricted our simulations to only the (110) oriented tantalum surface because it has the most thermodynamically stable surface energy (taking into account the relatively small size of our model surface), when compared to other planes.[49] A 4×4 slab super-cell with three carbon and two tantalum layers was used for all interface models. To ensure perfect uniaxial stress conditions, we utilized the periodic simulation box.

Analytical methods: An FEI Quanta FEG 250 Scanning Electron Microscope (SEM) with 10kV beam accelerating voltage, SE-ETD detector (secondary electron - Everhart-Thornley detector) and high vacuum mode (pressure 10^{-4} Pa) was used to observe the B:CNW surface. The surface morphology data were evaluated by using the image analysis software package (Gwyddion, 2.40, Czech Republic). Grain sizes were determined using Image J (ImageJ, US National Institutes of Health, Bethesda, MD) by counting a minimum of 250 grains. The surface topography was examined with an atomic force microscope (AFM) (Veeco Nanoman V, Veeco Instruments Inc., New York, NY, USA) in tapping mode. The imaging tapping mode and standard Si tips were used to perform the surface characterization. The scan size was 2× 2 μm.

Raman spectra were measured in a Renishaw InVia spectrometer with Spectra-Physics 532 nm solid state laser in combination with a 100x objective magnification (NA = 0.95) and 50 μm confocal aperture. The relative sp^3/sp^2 band ratios were determined by deconvolution of Raman spectra with the use of Gramms/AI Suite (ThermoScientific, USA) and subsequent comparison of integral intensity of a band assigned to diamond (approx. 1332 cm^{-1}) and a wide "G" band assigned to a distorted sp^2 phase (between 1520 and 1600 cm^{-1}).

Spectroscopic ellipsometry investigations were carried out with a phase-modulated ellipsometer Jobin-Yvon UVISEL (HORIBA Jobin-Yvon Inc., Edison, USA). The investigated wavelength region was 250–800 nm with a step of less than 0.5 nm. The experiments were carried out at room temperature using an angle of incidence fixed at 60° and the compensator set at 45°. The incidence angle resulted from the Brewster's angle of quartz glass substrate. DeltaPsi software (v. 2.4.3) was employed to determine the spectral distributions of refractive index n (λ) and extinction coefficient k (λ) of the diamond films.

The diamond sheets transferred to thick oxide wafer (200 nm SiO_2 thickness) were studied by the 4-point probe method to characterize their electrical properties. Prior to measurement, Ohmic contacts (Ti/Au) were deposited on the diamond samples. The resistivity was measured on the both sides of diamond nanosheets at room temperature by a four-point probe with an interprobe spacing of s=1.5 mm and needle probes with a 100 μm diameter. Samples were 1 x 1 cm in size. Due to finite sample size, the correction factor of 0.86 was taken into account during resistivity estimation.[50,51] A source meter (Keithley 2400, UK) was utilized as a current source applied to the external probes. The current was gradually increased from 0 up to 100μA with a step of 1μA. Voltage on the internal probes was measured with a multimeter (Appa 207, Taiwan). Each sample was measured 10 times at four various surface points, and the mean resistivity was calculated. The Hall effect measurements were performed in a 0.5 T magnetic field in the van der Pauw geometry. Four ohmic contacts were deposited close to the corners of each sample. The values of mobility and carrier density on the top and back sides of the diamond nanosheet were part investigated in detail.

The process of heterojunction fabrication: The CVD grown graphene was transferred onto a Si/SiO_2 chip (200 nm SiO_2 thickness). The as-grown diamond were annealed in air at 200ºC to obtain oxygen termination at both sides of diamond sheets. Next, diamond sheets were mechanically downsized with tweezers and positioned onto Elvacite acrylic resin/scotch tape/glass slide stack to fit them to the nanosized CVD graphene flakes. The spin coating parameters for Elvacite polymer were 4000 rpm for 1 min at 1000 rpm/s acceleration. The stack was baked at 110°C for 10 min on a hot plate in the air. During the transfer process, the diamond nanosheets were positioned such that half of the sheet ended up on CVD graphene layer, while the other half was in direct contact with the SiO_2 surface avoiding contact with the CVD graphene. The next fabrication step consisted of using Electron Beam Lithography on a 1.5 μm

spin-coated PMMA polymer baked at 180℃ for 10 min. The Ohmic metal contacts (5nm Ti and 400nm Au) were deposited on the device by using electron beam evaporator (Temescal, BJD-1800).

Acknowledgements
The authors gratefully acknowledge the financial support from the Polish National Science Centre (NCN) under Grant No. 2015/16/T/ST7/00469, 2016/21/B/ST7/01430, 2016/22/E/ST7/00102, 2014/14/M/ST5/00715 and the National Centre for Science and Development Grant Techmatstrateg No. 347324. This work was partially supported by the US DOE (DE-SC0014607) and by the Science for Peace Programme of NATO (Grant no. G5147). The DS funds of the Faculty of Electronics, Telecommunications, and Informatics of the Gdansk University of Technology are also acknowledged.

Received: ((will be filled in by the editorial staff))

Revised: ((will be filled in by the editorial staff))

Published online: ((will be filled in by the editorial staff))

References

[1] R. Bogdanowicz, M. Śmietana, M. Gnyba, M. Ficek, V. Straňák, Ł. Goluński, M. Sobaszek, J. Ryl, *Phys. Status Solidi A* **2013**, *210*, 1991.
[2] M. Smietana, J. Szmidt, M. L. Korwin-Pawlowski, W. J. Bock, J. Grabarczyk, *Diam. Relat. Mater.* **2007**, *16*, 1374.
[3] A. Aleksov, M. Kubovic, N. Kaeb, U. Spitzberg, A. Bergmaier, G. Dollinger, T. Bauer, M. Schreck, B. Stritzker, E. Kohn, *Diam. Relat. Mater.* **2003**, *12*, 391.
[4] V. A. Kukushkin, S. A. Bogdanov, *Diam. Relat. Mater.* **2015**, *60*, 94.
[5] Y. Wu, Y. Lin, A. A. Bol, K. A. Jenkins, F. Xia, D. B. Farmer, Y. Zhu, P. Avouris, *Nature* **2011**, *472*, 74.
[6] V. Seshan, J. O. Island, R. van Leeuwen, W. J. Venstra, B. H. Schneider, S. D. Janssens, K. Haenen, E. J. R. Sudhölter, L. C. P. M. de Smet, H. S. J. van der Zant, G. A. Steele, A. Castellanos-Gomez, *Nanotechnology* **2015**, *26*, 125706.
[7] A. Behroudj, S. Strehle, in *Micro-Nano-Integr. 6 GMM-Workshop*, **2016**, pp. 1–4.
[8] M. A. Lodes, S. M. Rosiwal, R. F. Singer, *Key Eng. Mater.* **2010**, *438*, 163.
[9] J. Fecher, M. Wormser, S. M. Rosiwal, *Diam. Relat. Mater.* **2016**, *61*, 41.
[10] M. A. Lodes, S. Sailer, S. M. Rosiwal, R. F. Singer, *Appl. Surf. Sci.* **2013**, *282*, 335.
[11] F. S. Kachold, M. A. Lodes, S. M. Rosiwal, R. F. Singer, *Acta Mater.* **2013**, *61*, 7000.
[12] S. Sobolewski, M. A. Lodes, S. M. Rosiwal, R. F. Singer, *Surf. Coat. Technol.* **2013**, *232*, 640.
[13] M. Engenhorst, J. Fecher, C. Notthoff, G. Schierning, R. Schmechel, S. M. Rosiwal, *Carbon* **2015**, *81*, 650.
[14] N. W. Winter, F. H. Ree, *J. Comput.-Aided Mater. Des.* **1998**, *5*, 279.

[15] W.-L. Yan, M. Sygnatowicz, G.-H. Lu, F. Liu, D. K. Shetty, *Surf. Sci.* **2016**, *644*, 24.
[16] S. Lee, W. M. Sigmund, *Colloids Surf. Physicochem. Eng. Asp.* **2002**, *204*, 43.
[17] J. W. Edwards, R. Speiser, H. L. Johnston, *J. Appl. Phys.* **1951**, *22*, 424.
[18] G. A. Slack, S. F. Bartram, *J. Appl. Phys.* **1975**, *46*, 89.
[19] J. Rumble, Ed. , *CRC Handbook of Chemistry and Physics, 98th Edition*, CRC Press, **2017**.
[20] M. Tsigkourakos, T. Hantschel, C. Bangerter, W. Vandervorst, *Phys. Status Solidi A* **2014**, *211*, 2284.
[21] A. Gicquel, K. Hassouni, F. Silva, J. Achard, *Curr. Appl. Phys.* **2001**, *1*, 479.
[22] F. Pinzari, P. Ascarelli, E. Cappelli, G. Mattei, R. Giorgi, *Diam. Relat. Mater.* **2001**, *10*, 781.
[23] L. Ostrovskaya, V. Perevertailo, V. Ralchenko, A. Dementjev, O. Loginova, *Diam. Relat. Mater.* **2002**, *11*, 845.
[24] R. Bogdanowicz, A. Fabianska, L. Golunski, M. Sobaszek, M. Gnyba, J. Ryl, K. Darowicki, T. Ossowski, S. D. Janssens, K. Haenen, E. M. Siedlecka, *Diam. Relat. Mater.* **2013**, *39*, 82.
[25] S. Prawer, R. J. Nemanich, *Philos. Trans. R. Soc. Lond. Math. Phys. Eng. Sci.* **2004**, *362*, 2537.
[26] M. A. Prelas, G. Popovici, L. K. Bigelow, Eds. , *Handbook of Industrial Diamonds and Diamond Films*, CRC Press, New York, **1997**.
[27] A. C. Ferrari, J. Robertson, *Phys. Rev. B* **2001**, *63*, 121405.
[28] M. Rudigier, R. Haubner, *Anal. Bioanal. Chem.* **2012**, *403*, 675.
[29] A. Zieliński, R. Bogdanowicz, J. Ryl, L. Burczyk, K. Darowicki, *Appl. Phys. Lett.* **2014**, *105*, 131908.
[30] M. Tsigkourakos, T. Hantschel, Z. Xu, B. Douhard, J. Meersschaut, Y. Zou, K. Larsson, M. Boman, W. Vandervorst, *Phys. Status Solidi A* **2015**, *212*, 2595.
[31] J. C. Richley, J. N. Harvey, M. N. R. Ashfold, *J. Phys. Chem. C* **2012**, *116*, 18300.
[32] H. Li, T. Zhang, L. Li, X. Lü, B. Li, Z. Jin, G. Zou, *J. Cryst. Growth* **2010**, *312*, 1986.
[33] Y.-G. Lu, S. Turner, J. Verbeeck, S. D. Janssens, P. Wagner, K. Haenen, G. Van Tendeloo, *Appl. Phys. Lett.* **2012**, *101*, 041907.
[34] D. Chateigner, F. Brunet, A. Deneuville, P. Germi, M. Pernet, E. Gheeraert, P. Gonon, *J. Cryst. Growth* **1995**, *148*, 110.
[35] S. Zhao, K. Larsson, *J. Phys. Chem. C* **2014**, *118*, 1944.
[36] G. Zhang, S. D. Janssens, J. Vanacken, M. Timmermans, J. Vacík, G. W. Ataklti, W. Decelle, W. Gillijns, B. Goderis, K. Haenen, P. Wagner, V. V. Moshchalkov, *Phys. Rev. B* **2011**, *84*, 214517.
[37] J. Yu, G. Liu, A. V. Sumant, V. Goyal, A. A. Balandin, *Nano Lett.* **2012**, *12*, 1603.
[38] B. Massarani, J. C. Bourgoin, R. M. Chrenko, *Phys. Rev. B* **1978**, *17*, 1758.
[39] R. Bogdanowicz, M. Sobaszek, J. Ryl, M. Gnyba, M. Ficek, Ł. Gołuński, W. J. Bock, M. Śmietana, K. Darowicki, *Diam. Relat. Mater.* **2015**, *55*, 52.
[40] D. Sholl, J. A. Steckel, *Density Functional Theory: A Practical Introduction*, John Wiley & Sons, **2011**.
[41] M. Griebel, J. Hamaekers, *Comput. Methods Appl. Mech. Eng.* **2004**, *193*, 1773.
[42] M. Griebel, S. Knapek, G. Zumbusch, *Numerical Simulation in Molecular Dynamics: Numerics, Algorithms, Parallelization, Applications*, Springer Science & Business Media, **2007**.
[43] H. J. Monkhorst, J. D. Pack, *Phys. Rev. B* **1976**, *13*, 5188.
[44] S. Plimpton, *J. Comput. Phys.* **1995**, *117*, 1.

[45] K. D. Nielson, A. C. T. van Duin, J. Oxgaard, W.-Q. Deng, W. A. Goddard, *J. Phys. Chem. A* **2005**, *109*, 493.
[46] L. Liu, A. Jaramillo-Botero, W. A. Goddard, H. Sun, *J. Phys. Chem. A* **2012**, *116*, 3918.
[47] An, Q., Jaramillo-Botero, A., Goddard III, W.A., California Institute of Technology, Pasadena, **2010**.
[48] E. A. Ekimov, V. A. Sidorov, E. D. Bauer, N. N. Mel'nik, N. J. Curro, J. D. Thompson, S. M. Stishov, *Nature* **2004**, *428*, 542.
[49] L. Vitos, A. V. Ruban, H. L. Skriver, J. Kollár, *Surf. Sci.* **1998**, *411*, 186.
[50] Haldor Topsøe Semiconductor Division, *Geometric Factors in Four Point Resistivity Measurement.*, Available For Download From Bridge Technology Website Http://Four-Point-Probes.Com/Haldor.Html, **1968**.
[51] F. M. Smits, *Bell Syst. Tech. J.* **1958**, *37*, 711.

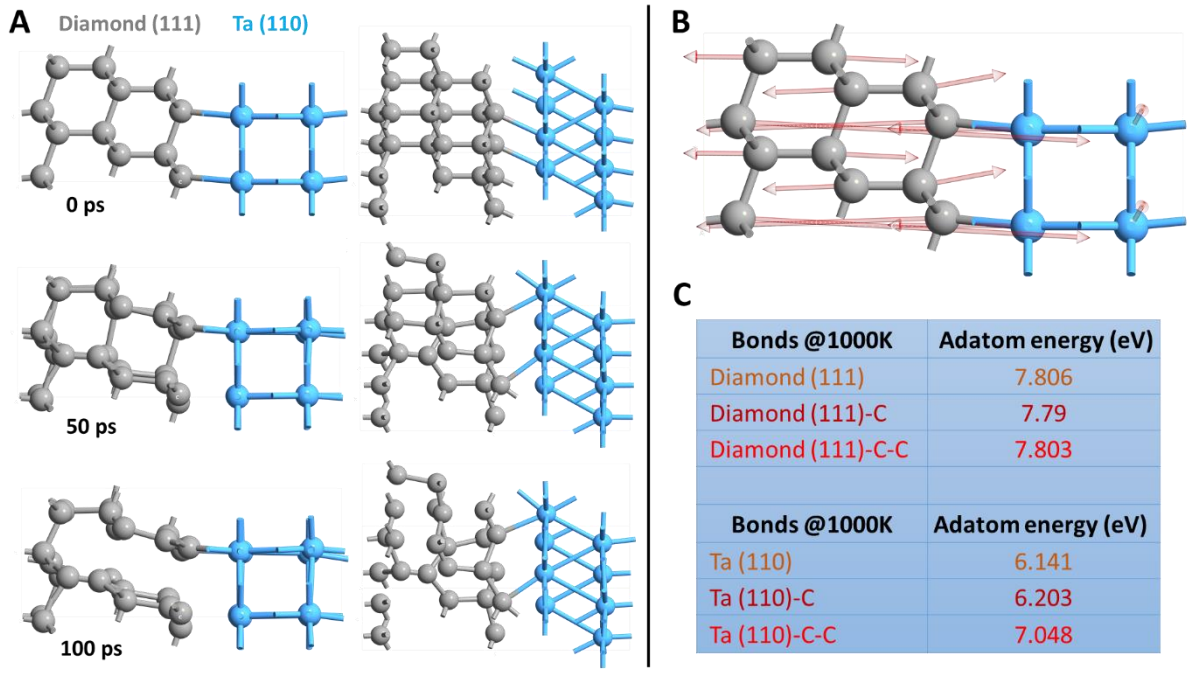

Bonds @1000K	Adatom energy (eV)
Diamond (111)	7.806
Diamond (111)-C	7.79
Diamond (111)-C-C	7.803
Bonds @1000K	**Adatom energy (eV)**
Ta (110)	6.141
Ta (110)-C	6.203
Ta (110)-C-C	7.048

Figure 1. Mechanism of diamond nanosheet delamination at the tantalum substrate simulated by molecular dynamics methods: (A) molecular dynamics of interface during thermal stress, (B) directions of forces in the atomic structure, (C) covalent bond energies of Ta-C and C-C lattices.

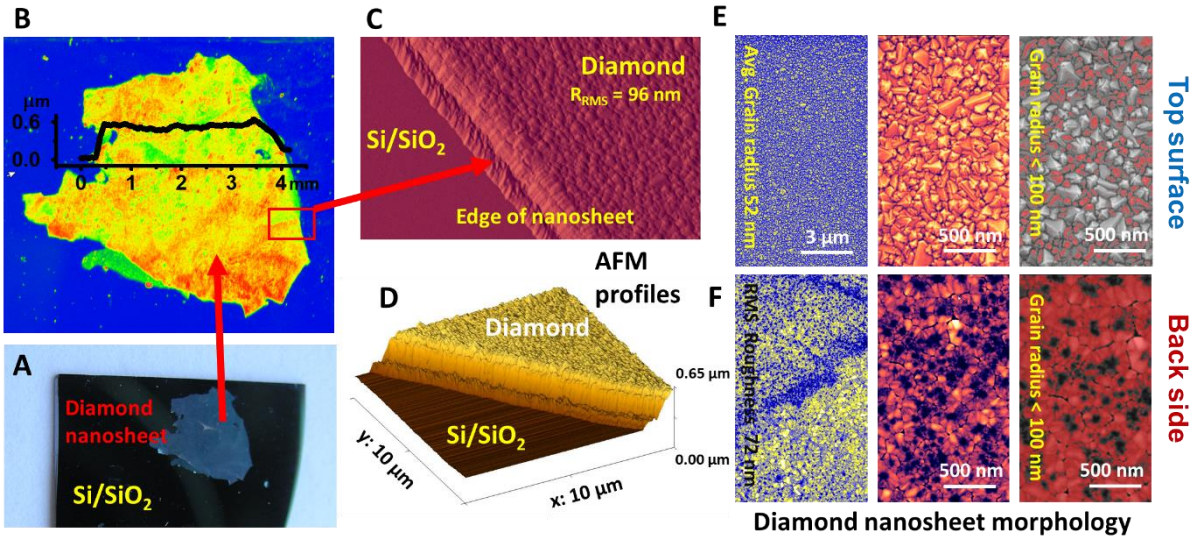

Figure 2. The surface morphology and profile of diamond sheets: (A) transferred fragment of diamond sheet; (B) sample profile; (C) and (D) AFM profiles of diamond sheets transferred to SiO_2 substrate; (E) SEM micrographs of the top surface of diamond sheet; (F) SEM micrographs of the back side of diamond sheet.

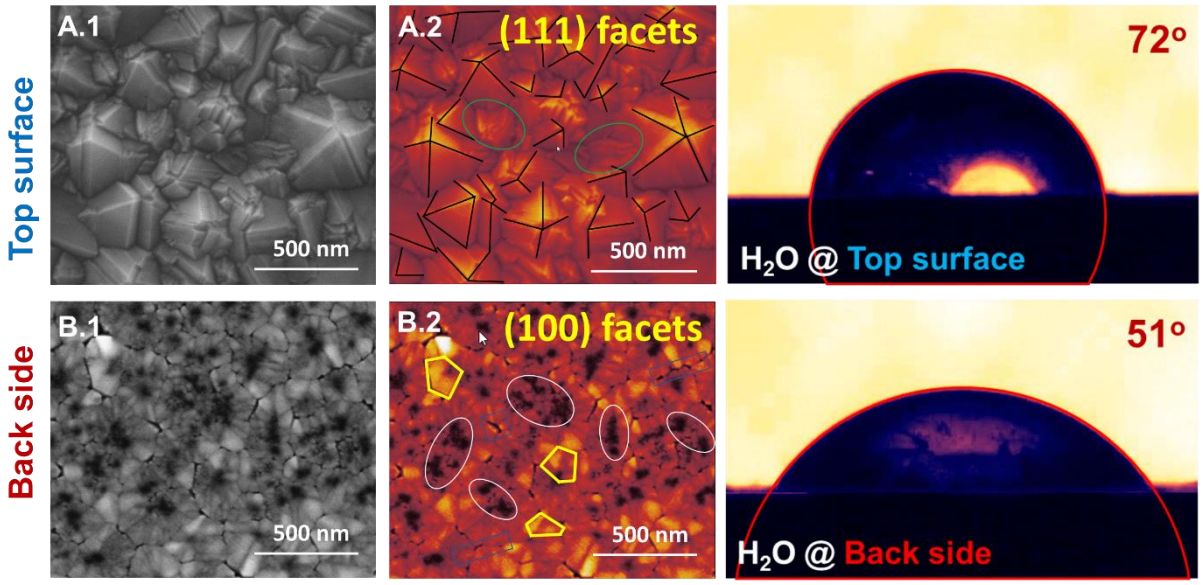

Figure 3. Morphology, the contribution of crystal facets and wetting properties of the top and back sides of diamond nanosheets.

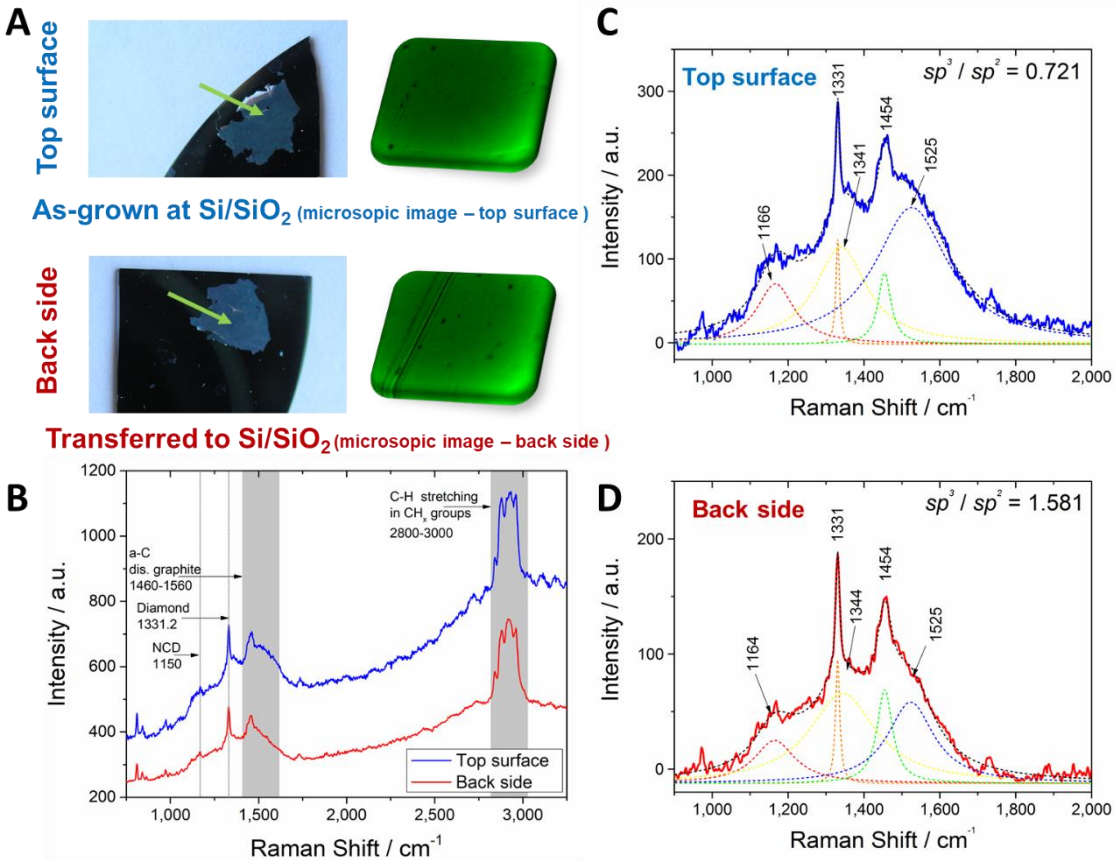

Figure 4. Raman spectra of boron-doped diamond sheets ([B]/[C]= 10000 ppm) deposited at the tantalum substrate and transferred to thick oxide wafer: (A) photos of the samples, (B) Raman spectra of the both sides of diamond nanosheet, (C) top surface, and (D) bottom surface.

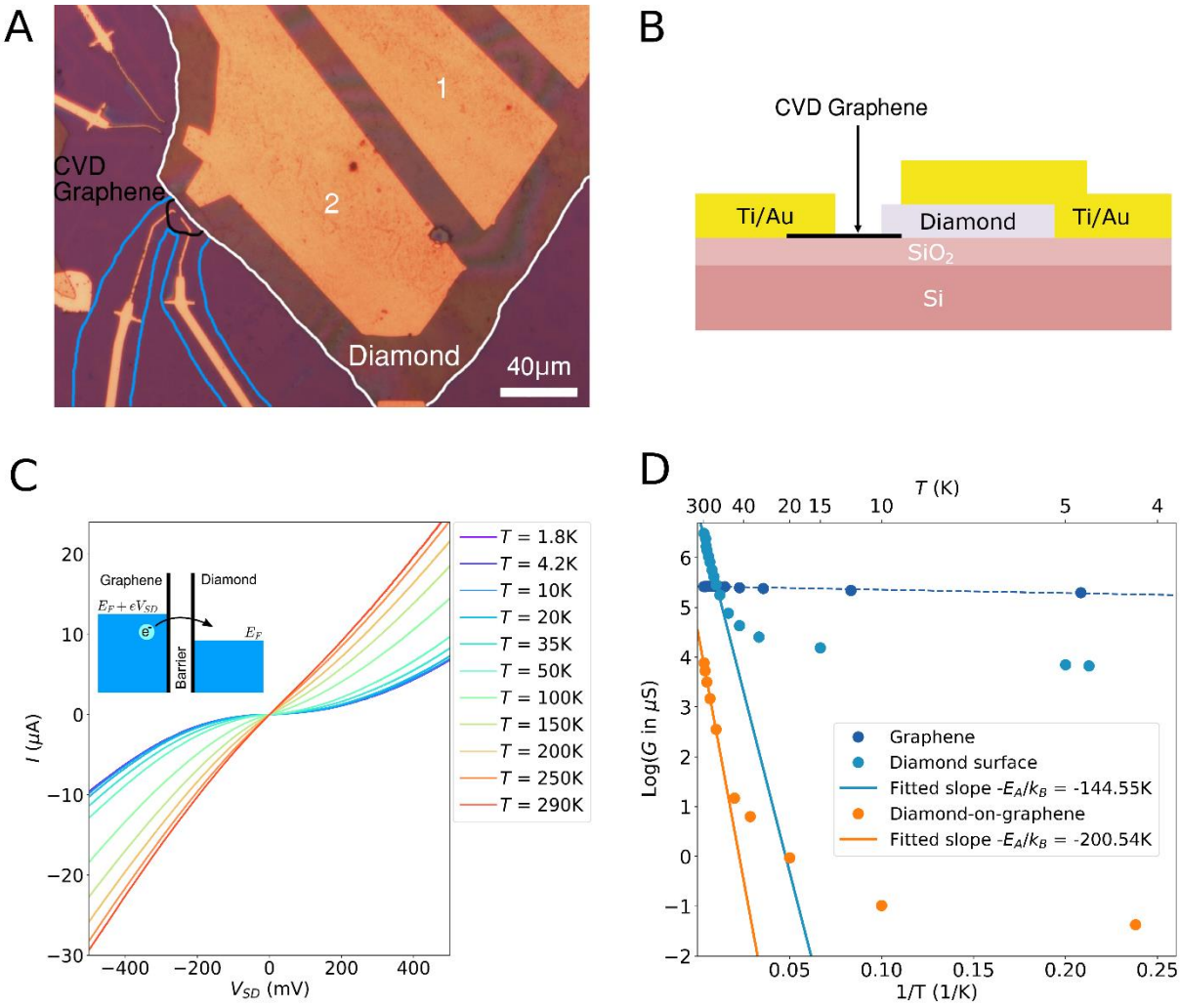

Figure 5. (A) Optical image of a diamond-on-graphene heterojunction (the diamond nanosheet is marked by a white line, the CVD graphene islands by a black line, and evaporated contacts by a blue line). The blue lines also indicate the region where the graphene islands have been cut by etching away a narrow area to avoid crosscurrents. (B) Schematic diagram of sample, a side-view. (C) Temperature-dependent *I-V* characteristics of a diamond-on-graphene heterojunction. Top left inset: Illustration of the tunneling behavior at the heterojunction under low-*T* and low-bias conditions. (D) Logarithm of conductance *G* vs. 1/*T* for the low bias *I-V* curves (top axes for T in K is included for readability). The data shows a graphene sample, a diamond sample and a diamond-on-graphene heterojunction.

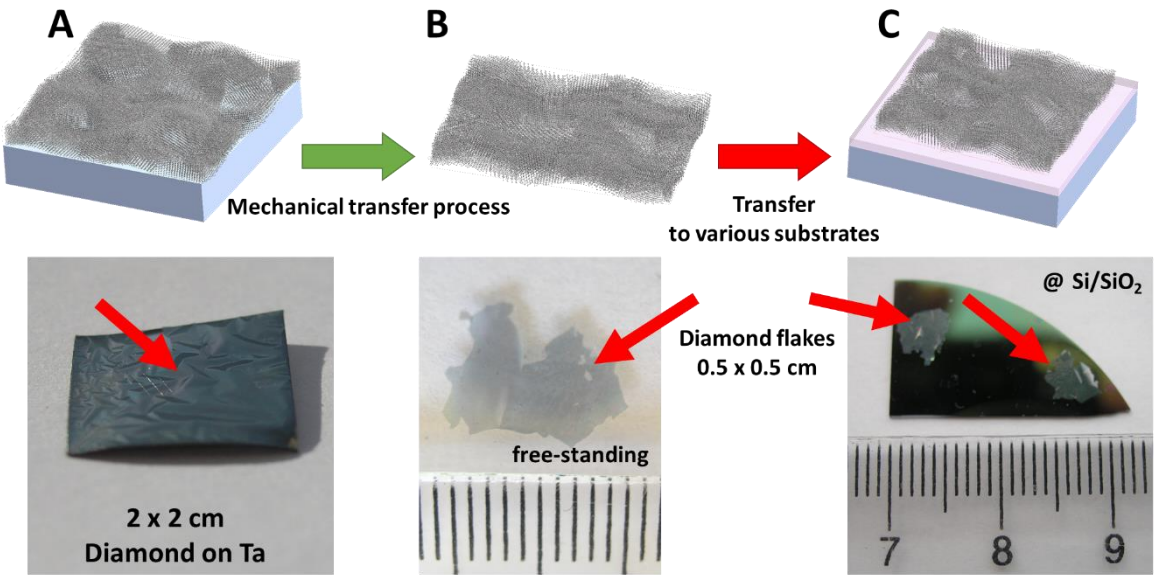

Figure 6. Schematic representation of the isolation and transfer of diamond nanosheets.

Table 1. Electronic and electrochemical parameters of the diamond nanosheet.

Diamond nanosheet	Charge carrier density (#/cm^3)	Hall mobility (cm^2/Vs)	Resistivity (Ω cm)
Top surface	3.1×10^{17}	62	0.32
Back side	1.67×10^{14}	532	71